Quantum interface of an electron and a nuclear ensemble

D. A. Gangloff,[1*†] G. Éthier-Majcher,[1*‡] C. Lang,[1] E. V. Denning,[1,2] J. H. Bodey,[1]
D. M. Jackson,[1] E. Clarke,[3] M. Hugues,[4] C. Le Gall,[1] M. Atatüre[1†]

[1]Cavendish Laboratory, University of Cambridge,
JJ Thomson Avenue, Cambridge CB3 0HE, United Kingdom
[2]Department of Photonics Engineering, Technical University of Denmark,
2800 Kgs. Lyngby, Denmark
[3]EPSRC National Epitaxy Facility, University of Sheffield,
Broad Lane, Sheffield, S3 7HQ, United Kingdom
[4]Université Côte d'Azur, CNRS, CRHEA,
rue Bernard Gregory, 06560 Valbonne, France

[*]These authors contributed equally to this work
[†]To whom correspondence should be addressed: dag50@cam.ac.uk, ma424@cam.ac.uk.

Coherent excitation of an ensemble of quantum objects underpins quantum many-body phenomena, and offers the opportunity to realize a memory that stores quantum information. Thus far, a deterministic and coherent interface between a spin qubit and such an ensemble has remained elusive. Here, we first use an electron to cool the mesoscopic nuclear-spin ensemble of a semiconductor quantum dot to the nuclear sideband-resolved regime. We then implement an all-optical approach to access individual quantized electronic-nuclear spin transitions. Finally, we perform coherent optical rotations of a single collective nuclear spin excitation – a spin wave. These results constitute the building blocks of a dedicated local memory per quantum-dot spin qubit and promise a solid-state platform for quantum-state engineering of isolated many-body systems.

[‡] Present address: Anyon Systems Inc., 1985 55e Avenue #100, Dorval, QC H9P 1G9, Canada

A controllable quantum system provides a versatile interface to observe and manipulate the quantum properties of an isolated many-body system (*1*). In turn, collective excitations of this ensemble can store quantum information as a memory (*2, 3*) – a contemporary challenge for quantum technologies. While a number of hybrid qubit-ensemble approaches have been pursued in the last decade (*4, 5*), nuclear spins remain the most promising ensemble candidate owing to their unparalleled coherence times. Such a nuclear ensemble interfaced with a (spin) qubit is described elegantly by the central spin model (*6,7*), studied in donor atoms embedded in Si (*8,9*), diamond color centers (*10–12*), and semiconductor nanostructures (*13–16*). In these systems, the state of the central spin and of the spin ensemble that surrounds it are tied by mutual interaction, allowing proxy control over the many-body system and long-lived storage in principle (*2*). Realising this scenario with an electron in a semiconductor quantum dot (QD) offers access to a large ensemble of nuclear spins with quasi-uniform coupling to the central spin. In this system, coherent addressing of the ensemble via the central spin has yet to be shown, and a limiting factor is the thermal fluctuations of the surrounding spins that obfuscate the state-selective transitions required for such control. However, driving the central spin can stimulate exchange of energy with its surrounding spins, and thus modify the properties of its own environment. This has been shown to reduce the uncertainty on the collective spin state of the isolated QD nuclei, leading to prolonged electron spin coherence (*17–21*).

In this Report, we use all-optical stimulated Raman transitions to manipulate the electron-nuclear system and realize a coherent interface. First employing a configuration analogous to Raman cooling of atoms (*22*), we drive the electron spin to reduce the thermal fluctuations of the nuclear spin ensemble (Fig. 1a). Cooling the nuclear spin fluctuations to an effective temperature well below the nuclear Zeeman energy (< 1 mK), followed immediately by detuned probing of the electron spin resonance (ESR), we reveal an excitation spectrum of transitions between many-body states that are collectively enhanced by the creation of a single nuclear spin-wave excitation – a nuclear magnon. Finally we drive a single magnon transition resonantly, inducing coherent exchange between the electron spin and the nuclear spin ensemble.

Our system consists of a charge-controlled semiconductor QD (*23*), where a single electron spin is coupled optically to a charged exciton state, and magnetically to an isolated reservoir of N (10^4 to 10^5) nuclear spins of As (total spin $I = 3/2$), Ga ($I = 3/2$), and In ($I = 9/2$), as in Fig. 1b. We drive the electron-nuclear system with a narrow two-photon resonance at detuning δ from an excited state, whose linewidth Γ is tunable via the optical pumping rate of the electron spin (Fig. 1b), as with Raman cooling (*22*). The optical parameters set the dissipation rate relative to the energy scales relevant for cooling, which are the nuclear Zeeman energy ω_n and the hyperfine coupling energy per nucleus A_c, like the phonon and photon recoil energies for trapped atoms (*22*). In atomic physics, the motion of an atom relative to detuned driving fields leads to a velocity-dependent absorption rate via the Doppler effect and, together with the photon recoil momentum, to a damping force that is the basis of laser cooling of atomic motion (*24*). In our system, the hyperfine interaction between the electron and nuclei leads to a shift of the ESR that depends linearly on the net polarization I_z of the nuclei (*6*); this Overhauser shift $2A_\mathrm{c}I_\mathrm{z}$ thus leads to a polarization-dependent absorption rate. In the presence of material strain, the hyperfine interaction enables optically driven nuclear spin flips that can be modelled as sidebands of amplitude $\eta\Omega$ ($\eta < 1$) on a principal transition of amplitude Ω that flips the electron spin only (*25, 26*). With fast electron spin reset, absorption on the sidebands at polarization-dependent rates $W_\pm(I_\mathrm{z})$ can increase ($+$) or decrease ($-$) the mean nuclear polarization I_z, as shown in Fig. 1c, in a process known as dynamic nuclear polarization (*6, 27*). The evolution of this complex system pitting drift $W_\pm$ against diffusion $\Gamma_\mathrm{d}(I_z)$ is captured elegantly by a simple rate equation (*26, 28*):

$$\frac{dI_\mathrm{z}}{dt} = -\frac{\Gamma_\mathrm{tot}}{(3N/2)}\left[I_z - f(I_z)\right], \tag{1}$$

where $\Gamma_\mathrm{tot} = W_+ + W_- + \Gamma_\mathrm{d}$ is the total diffusion rate, and $f(I_z) = (3N/2)(W_+ - W_-)/\Gamma_\mathrm{tot}$ is the cooling function that reduces fluctuations, as in Doppler cooling (*24*). The polarization $I_0 = \delta/(2A_\mathrm{c})$ is the steady-state of the dynamical system defined by Eq. 1, as shown in Fig. 1c. Rate extrema occur when the Overhauser shift brings a sideband transition in resonance with the drive, $|2A_\mathrm{c}(I_\mathrm{z} - I_0)| \approx \omega_\mathrm{n}$ (for $\omega_\mathrm{n} \gg A_\mathrm{c}$), suggesting that Overhauser fluctuations can be reduced below the nuclear Zeeman energy, ω_n. The driven ensemble experiences damping proportional to the cooling-function gradient, $(5/3)f'(I_0)$. For a probability distribution $p(I_\mathrm{z})$, the fluctuations ΔI_z^2 are reduced from their thermal-equilibrium value $5N/4$ (Fig. 1c) by (*23, 28*)

$$\frac{\Delta I_\mathrm{z}^2}{5N/4} = \frac{1 - \left(\frac{2}{5N}I_0\right)^2}{1 - \frac{5}{3}f'(I_0)}. \tag{2}$$

From the electron's perspective, a commensurate reduction of fluctuations occurs for a highly polarized nuclear ensemble, which to-date has not been achieved. This occurs at thermal equilibrium when the energy $k_\mathrm{B}T$ falls below the system's defining energy scale, here the nuclear Zeeman energy $\hbar\omega_\mathrm{n}$. The fluctuations in Fig. 1c thus correspond to an effective temperature below $T = \hbar\omega_\mathrm{n}/k_\mathrm{B} = 1$ mK (*23*).

Figure 2 highlights the optimal conditions for cooling the nuclear ensemble. The electron coherence time T_2^* is a direct measure of nuclear polarization fluctuations $\Delta I_\mathrm{z}^2 = 1/2(A_\mathrm{c}T_2^*)^2$ (*21, 23*), therefore Ramsey interferometry on the electron spin (*29, 30*) serves as our thermometer. We parametrize temperature as a cooling performance factor $(5N/4)/\Delta I_z^2$ as a function of Raman rate Ω and excited-state

linewidth Γ, as shown in Fig. 2a. A maximum of $\sim$300 is found where the Raman rate $\Omega = 17$ MHz is approximately half of the nuclear Zeeman splitting $\omega_{\rm n} = 36$ MHz, and the excited-state linewidth corresponds to optical saturation, $\Gamma \sim 25$ MHz. This is in quantitative agreement with our theoretical prediction, shown in Fig. 2b, that accounts for nuclear-spin diffusion and inhomogeneous broadening (*23*).

The Raman rate Ω and the electronic excited-state linewidth Γ determine the spectral selectivity and the diffusion rate of the cooling process. For best cooling, no absorption should occur at the stable point I_0, while sideband absorption should turn on sharply in response to polarization fluctuations away from I_0. Optimal values for Ω and Γ thus depend on the sideband spacing $\omega_{\rm n}$: $\Omega, \Gamma \ll \omega_{\rm n}$ entails high spectral selectivity but weak sideband absorption near I_0, while $\Omega, \Gamma \sim \omega_{\rm n}$ entails strong absorption on the sidebands but low spectral selectivity. Figure 2c depicts this dependence of the cooling function $f(I_{\rm z})$ on the optical parameters: the damping $f'(I_0)$ is largest when the Raman rate is approximately half of the nuclear Zeeman energy, $\Omega \sim \omega_{\rm n}/2$, and when close to saturation $\Omega \sim \Gamma/\sqrt{2}$. We confirm this experimentally in Fig. 2d by changing the applied magnetic field: the values of Ω and Γ that optimize the cooling performance are proportional to the sideband spacing.

The lowest temperature of our system is a function of distinct diffusion and broadening processes competing with Raman cooling, through magnetic-field dependent rates: in the low-field regime, homogeneous broadening of the ESR dominates (*29, 30*) (purple region in Fig. 2e), while in the high-field regime optical diffusion does (*23*) (red region in Fig. 2e). Further, electron-mediated nuclear spin diffusion (*31, 32*) counteracts Raman cooling in both regimes. Figure 2e displays the magnetic field dependence of the temperature optimized against optical parameters. Our results follow closely the field-dependent bounds obtained from modelling the diffusion processes (solid curve), and establish the globally optimal cooling performance of $\sim$400 at $\sim$3.3 T. Operating close to this field, we prepare the nuclear ensemble at an effective temperature of 200 μK (*23*). There, the Overhauser fluctuations are well below the nuclear Zeeman splitting, $2A_{\rm c}\sqrt{\Delta I_{\rm z}^2} = 7$ MHz $< \omega_{\rm n} = 22$ MHz (at 3 T), which places our system well into the sideband-resolved regime.

We now probe the electron-spin state in the coherent regime where dissipation is turned off, $\Gamma \to 0$. We drive the ESR for a time τ at a detuning δ and measure the electron $|{\downarrow}\rangle$ population (Fig. 3a). Figure 3b shows this time-resolved spectrum obtained from our theoretical analysis (*23*), where we expect five distinct processes, as shown in Fig. 3c: a central transition at $\delta = 0$, and four sideband transitions at $\delta = \pm\omega_{\rm n}, \pm 2\omega_{\rm n}$. The nuclear spin-flip transitions originate from the strain-induced electric field gradient that couples to the quadrupole moment of all QD nuclei, mixing their Zeeman eigenstates (*16*). The quadratic nature of this interaction allows the nuclear polarisation to change either by one quantum ($I_{\rm z} \to I_{\rm z} \pm 1$) (*25, 26*) or by two quanta ($I_{\rm z} \to I_{\rm z} \pm 2$); these selection rules apply to all QD nuclear spin species. A first-order perturbative expansion of the hyperfine interaction (*23*) dresses the ESR with these transitions. When the driving field with amplitude Ω is detuned from the principal transition by one or two units of nuclear Zeeman energy $\omega_{\rm n}$, these resonant transitions occur with an amplitude $\eta\Omega$, as sidebands of strength $\eta = \mathcal{D}A_{\rm nc}/\omega_{\rm n}$; here $A_{nc} \approx 0.015A_{\rm c}$ is the non-collinear hyperfine constant parametrizing the perturbation. The driven electron cannot distinguish the $\sim N$ possible spin-flips that take I_z to $I_z \pm 1, \pm 2$, which leads to the degeneracy factor $\mathcal{D} \sim \sqrt{N}$. This underpins the collective enhancement (*33*) that makes the nuclear spin-flip sideband transitions so prominent in our system.

Figure 3d shows the experimental spectra averaged over short delays $\tau = 0 - 150$ns, where $\Omega\tau \sim \pi$, revealing the principal ESR with optimal (violet data) and suboptimal (red data) cooling. The feature width is a convolution of the drive Rabi frequency Ω with the Overhauser field fluctuations $2A_{\rm c}\sqrt{\Delta I_{\rm z}^2}$, and highlights the spectral narrowing achieved by Raman cooling. Figure 3e shows the time-frequency map of this measurement. At $\delta = 0$, the principal ESR leads to Rabi oscillations at $\Omega = 3.8$ MHz. At larger delays where $\eta\Omega\tau \sim \pi$ and at a sufficient detuning from the principal transition $\delta \gg \Omega$, the emergence of four sideband processes agrees well with our predictions. Figure 3f is a standout observation of the sideband spectrum, integrated over $\tau = 850 - 1000$ns. A five-Gaussian fit (dashed curve) verifies that the sidebands emerge at integer multiples of ω_n, and the shaded area highlights the theoretical spectrum. Our results confirm that the sideband drive can excite selectively a single nuclear spin-flip in the ensemble and highlight that $\sim N$ sufficiently identical nuclei are simultaneously coupled to the driven electron. In contrast to magnons in ferromagnetic materials, this type of collective excitation is based on an electron-mediated interaction, in close analogy to photon-mediated magnon-polariton modes in strongly coupled light-matter interfaces (*3*). Until now, such a collective nuclear-spin excitation had only been observed as ensemble measurements of atomic gases (*34*) and magnetic materials (*35, 36*), while our result represents the deterministic generation of a single nuclear magnon by interfacing the nuclei with an elementary controllable quantum system.

This spectral selectivity enables coherent generation of a single-spin excitation, provided it is faster than the dephasing times of the electron [$T_2 \approx 1$ μs (*30*)] and the nuclei [$T_2 \approx 10$ μs (*32*)]. Figure 4 illustrates this coherent drive via Rabi oscillations. Detuning maximally from the quenching effect of coupling to the principal transition, we drive one of the second sidebands ($I_{\rm z} \to I_{\rm z} + 2$) with $\eta\Omega > 1/T_2$ (Fig. 3c), and measure for delays $\tau \gtrsim \pi/\eta\Omega$. Figure 4 presents measurements with three Rabi frequencies $\Omega = 7, 9, 12$ MHz (*23*). Oscillations of the electron spin population at a fraction η of the carrier frequency Ω are a direct measurement of coherent

electron-nuclear dynamics. We attribute the sharp appearance of oscillations above a Rabi frequency $\Omega \sim 10$ MHz to reaching a sufficient sideband coupling $\eta\Omega \sim 1.5$ MHz to overcome inhomogeneities, which exist on a MHz-scale within a more strongly coupled subset of nuclei (*23*). Our master equation model (solid lines in Fig. 4) captures this inhomogeneous broadening that limits the Rabi oscillations. The grey-shaded areas represent $\pm 20\%$ deviations of Rabi frequency, and our data's drift towards lower Rabi frequency at long delays suggests a dephasing mechanism that depends on accumulated phase $\Omega\tau$. Our model further allows us to reconstruct the nuclear-spin population transfer, where the effect of off-resonant excitation of the principal transition is not present, and shows that the electron spin population transfer is accompanied predominantly by nuclear spin population transfer (*23*).

The value $\eta \sim 15\%$, directly extracted from the coherent oscillations in Fig. 4, confirms the $\sim \sqrt{N}$ enhancement of the sideband transition strength arising from the collective nature of the magnon excitation. Indeed, owing to sufficient coupling homogeneity, the nuclei can be treated as an ensemble of $N = 30{,}000$ indistinguishable spins under the hyperfine interaction with the electron. Oscillations in Fig. 4 indicate the creation and retrieval of a coherent superposition of a single nuclear spin excitation among all spins, forming the basis of many-body entanglement as found for Dicke states (*33*). This occurs despite operating near zero polarization, where the degeneracy of nuclear states is maximal. Strikingly, this exchange of coherence is far from the bosonic approximation available for a fully polarized ensemble (*2*). Furthermore, an intermediate drive time $\eta\Omega\tau = \pi/2$ generates an inseparable coherent superposition state for the electron and the nuclei.

In this work, we have realized a coherent quantum interface between a single electron and 30,000 nuclei using light. Making use of the back-action of a single nuclear-spin flip on the electron, the development of a dedicated quantum memory per electron spin qubit in semiconductor QDs becomes viable. Future possibilities also include creating and monitoring tailored collective quantum states of the nuclear ensemble, such as Schrödinger cat states, by harnessing Hamiltonian engineering techniques.

References

1. L. Amico, R. Fazio, A. Osterloh, V. Vedral, *Rev. Mod. Phys.* **80**, 517 (2008).
2. J. M. Taylor, C. M. Marcus, M. D. Lukin, *Phys. Rev. Lett.* **90**, 206803 (2003).
3. K. S. Choi, A. Goban, S. B. Papp, S. J. van Enk, H. J. Kimble, *Nature* **468**, 412 (2010).
4. X. Zhu, *et al.*, *Nature* **478**, 221 (2011).
5. Y. Tabuchi, *et al.*, *Science (80-.).* **349**, 405 (2015).
6. A. Abragam, L. C. Hebel, *Am. J. Phys.* **29**, 860 (1961).
7. D. Stanek, C. Raas, G. S. Uhrig, *Phys. Rev. B* **90**, 064301 (2014).
8. R. de Sousa, S. Das Sarma, *Phys. Rev. B* **68**, 115322 (2003).
9. J. J. Pla, *et al.*, *Nature* **489**, 541 (2012).
10. L. Childress, *et al.*, *Science (80-.).* **314**, 281 (2006).
11. G. Balasubramanian, *et al.*, *Nat. Mater.* **8**, 383 (2009).
12. N. Kalb, *et al.*, *Science (80-.).* **356**, 928 (2017).
13. A. V. Khaetskii, D. Loss, L. Glazman, *Phys. Rev. Lett.* **88**, 186802 (2002).
14. I. A. Merkulov, A. L. Efros, M. Rosen, *Phys. Rev. B* **65**, 205309 (2002).
15. H. Bluhm, *et al.*, *Nat. Phys.* **7**, 109 (2011).
16. B. Urbaszek, *et al.*, *Rev. Mod. Phys.* **85**, 79 (2013).
17. D. Stepanenko, G. Burkard, G. Giedke, A. Imamoglu, *Phys. Rev. Lett.* **96**, 136401 (2006).
18. A. Greilich, *et al.*, *Science (80-.).* **317**, 1896 (2007).
19. D. J. Reilly, *et al.*, *Science (80-.).* **321**, 817 (2008).
20. X. Xu, *et al.*, *Nature* **459**, 1105 (2009).
21. G. Éthier-Majcher, *et al.*, *Phys. Rev. Lett.* **119**, 130503 (2017).
22. D. J. Heinzen, D. J. Wineland, *Phys. Rev. A* **42**, 2977 (1990).
23. Supplementary Information available online.
24. W. D. Phillips, *Rev. Mod. Phys.* **70**, 721 (1998).
25. C.-W. Huang, X. Hu, *Phys. Rev. B* **81**, 205304 (2010).
26. A. Högele, *et al.*, *Phys. Rev. Lett.* **108**, 197403 (2012).
27. B. Eble, *et al.*, *Phys. Rev. B* **74**, 081306 (2006).
28. W. Yang, L. J. Sham, *Phys. Rev. B* **88**, 235304 (2013).
29. A. Bechtold, *et al.*, *Nat. Phys.* **11**, 1005 (2015).
30. R. Stockill, *et al.*, *Nat. Commun.* **7**, 12745 (2016).
31. C. Latta, A. Srivastava, A. Imamoğlu, *Phys. Rev. Lett.* **107**, 167401 (2011).
32. G. Wüst, *et al.*, *Nat. Nanotechnol.* **11**, 885 (2016).
33. R. H. Dicke, *Phys. Rev.* **93**, 99 (1954).
34. B. R. Johnson, *et al.*, *Phys. Rev. Lett.* **52**, 1508 (1984).
35. G. Seewald, E. Hagn, E. Zech, *Phys. Rev. Lett.* **78**, 5002 (1997).
36. L. V. Abdurakhimov, Y. M. Bunkov, D. Konstantinov, *Phys. Rev. Lett.* **114**, 226402 (2015).
37. D. Press, T. D. Ladd, B. Zhang, Y. Yamamoto, *Nature* **456**, 218 (2008).
38. A. Greilich, *et al.*, *Nat. Phys.* **5**, 262 (2009).
39. A. R. Onur, C. H. van der Wal, *Phys. Rev. B* **98**, 165304 (2018).
40. I. T. Vink, *et al.*, *Nat. Phys.* **5**, 764 (2009).
41. H. Bluhm, S. Foletti, D. Mahalu, V. Umansky, A. Yacoby, *Phys. Rev. Lett.* **105**, 216803 (2010).
42. M. Issler, *et al.*, *Phys. Rev. Lett.* **105**, 267202 (2010).
43. C. M. Chow, *et al.*, *Phys. Rev. Lett.* **117**, 1 (2016).
44. D. Press, *et al.*, *Nat. Photonics* **4**, 367 (2010).
45. C. Bulutay, *Phys. Rev. B* **85**, 115313 (2012).
46. J. R. Schrieffer, P. A. Wolff, *Phys. Rev.* **149**, 491 (1966).
47. S. Bravyi, D. P. DiVincenzo, D. Loss, *Ann. Phys. (N. Y).* **326**, 2793 (2011).
48. B. Urbaszek, *et al.*, *Phys. Rev. B* **76**, 201301 (2007).
49. A. I. Tartakovskii, *et al.*, *Phys. Rev. Lett.* **98**, 026806 (2007).
50. P. Maletinsky, A. Badolato, A. Imamoglu, *Phys. Rev. Lett.* **99**, 056804 (2007).

51. J. Wesenberg, K. Mølmer, *Phys. Rev. A* **65**, 062304 (2002).

Acknowledgments: We thank Andreas Nunnenkamp and Guido Burkard for critical reading of the manuscript, and Robert Stockill for helpful discussions. **Funding:** ERC PHOENICS (617985), EPSRC NQIT (EP/M013243/1). Sample growth in EPSRC National Epitaxy Facility. D.A.G. acknowledges a St John's College Fellowship, G.É.-M. an NSERC Postdoctoral Fellowship, E.V.D. the Danish Council for Independent Research (DFF-4181-00416), and C.LG. a Royal Society Fellowship. **Author contributions:** D.A.G., G.E-M., C.LG., and M.A. conceived the experiments. D.A.G., G.E-M., C.L. and D.M.J. acquired and analysed data. D.A.G., G.E-M., and E.V.D. performed the theory and simulations. E.C. and M.H. grew the sample. D.A.G., G.E-M., E.V.D., J.H.B., D.M.J., C.LG., and M.A. prepared the manuscript. **Competing interests:** None declared. **Data and materials availability:** All data needed to evaluate the conclusions in the paper are present in the paper or the Supplementary Materials.

Supplementary Materials

Supplementary Text
Figs. S1 to S8
Tables S1 to S2
References *(37-51)*

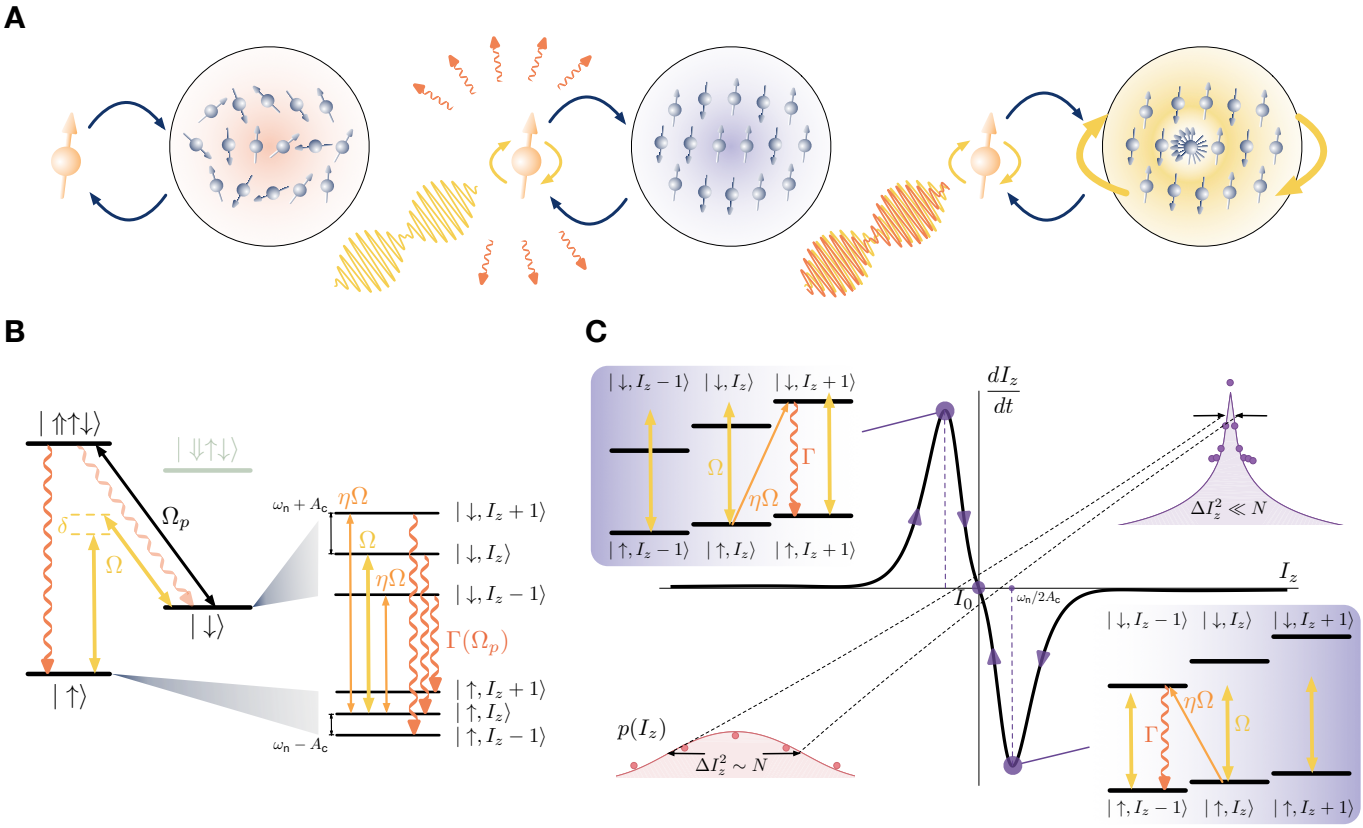

Figure 1: **An electron controls a nuclear ensemble (A)** The central spin scenario: (left) a spin interacts with a thermally fluctuating ensemble; (middle) in the presence of dissipation, the driven spin can cool the ensemble to a lower effective temperature; (right) driving the spin can create coherent superpositions of single spin-flips as collective excitations of the cooled ensemble. **(B)** Realization of this scenario in a semiconductor QD, under a magnetic field in Voigt geometry, optically pumped to electronic spin state $|\uparrow\rangle$ by a resonant drive Ω_p via the trion state $|\Uparrow\uparrow\downarrow\rangle$ of homogeneous linewidth $\Gamma_0 = 150$ MHz at a rate $\Gamma \sim \Omega_p^2/\Gamma_0 \leq 38$ MHz. The electron-spin splitting is (Overhauser) shifted by its hyperfine interaction $2A_c I_z$, where $A_c = 600$ kHz, with an ensemble of N (10^4 to 10^5) nuclear spins, described by mean polarization states $I_z = [-3N/2, 3N/2]$ (taken for spin-3/2). Far-detuned ($\gtrsim 1$ nm) Raman beams drive the electron spin resonance (ESR) at a Rabi frequency $\Omega \lesssim 40$ MHz, including transitions that simultaneously flip a single nuclear spin $I_z \to I_z \pm 1$ at frequency $\eta\Omega$ ($\eta < 1$). **(C)** Cooling dynamics: the time-derivative of polarization dI_z/dt depends on the polarization I_z, through the Overhauser shift and the nuclear-spin flipping transitions $W_\pm$. The polarization I_0 is the dynamical system's stable point, where the width ΔI_z^2 of the probability distribution $p(I_z)$ is reduced (violet) compared to its value without cooling (red).

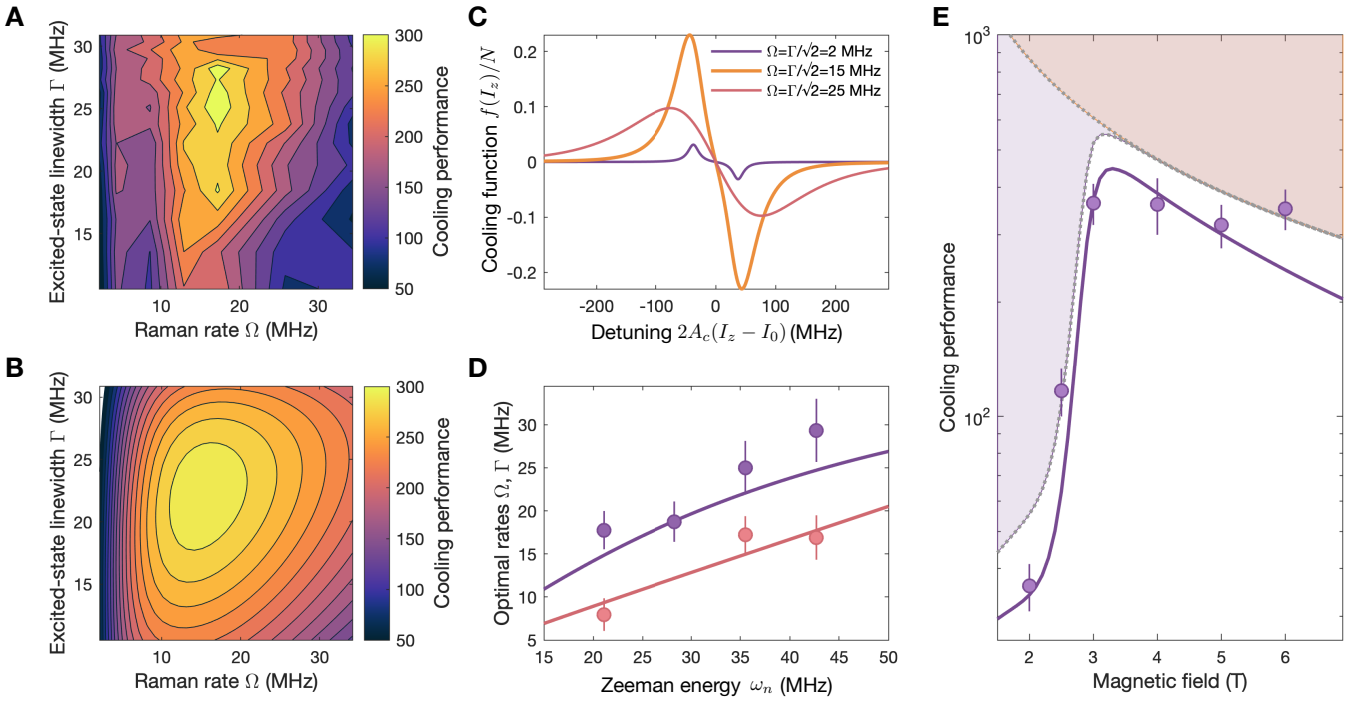

Figure 2: **Optimal cooling of the nuclear ensemble (A)** Experimental Raman cooling performance $5N/4\Delta I_z^2$ as a function of Raman rate Ω and excited-state linewidth Γ, at 5 T. The maximum of 300 is reached for $\Omega \sim \omega_n/2$, and saturation conditions $\Gamma \sim \sqrt{2}\Omega$. **(B)** Theoretical prediction of panel A. **(C)** Calculated cooling curves $f(I_z) \propto W_+ - W_-$ at optical saturation $\Omega = \Gamma/\sqrt{2}$ for increasing rates. The largest damping $f'(I_0)$ occurs when $\Omega \sim \omega_n/2 = 18$ MHz (orange curve). **(D)** Raman rate and excited-state linewidth at the measured optimal cooling performance as a function of ω_n at 3 T, 4 T, 5 T and 6 T. Solid curves are the corresponding theoretical calculations. **(E)** Magnetic-field optimal cooling. Circles represent the maximum cooling performance at a given magnetic field. Shaded regions are cooling limits, and curves from a theoretical model [see main text and (*23*)]. Error bars represent one standard deviation of uncertainty.

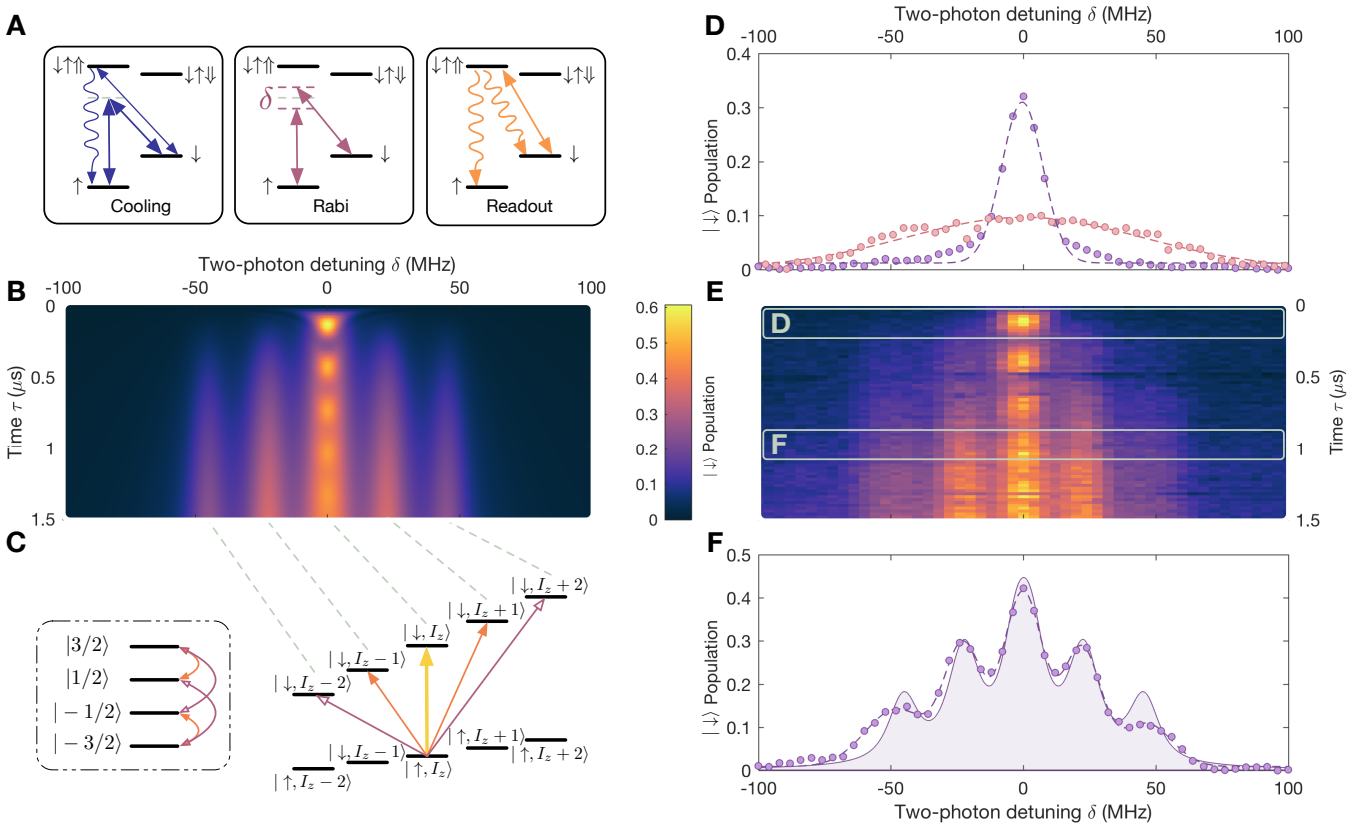

Figure 3: **Resolving single nuclear magnons (A)** Spectrum measurement sequence, from left to right: Raman cooling, Rabi drive ESR at detuning δ for time τ, and optical readout of the electron $|\downarrow\rangle$ population (*23*). **(B)** Theoretical ESR spectrum buildup as a function of two-photon detuning δ and drive time τ, for a Rabi frequency of $\Omega = 3.3$ MHz on the central transition. Sideband coupling η is fitted (*23*). The model is a master equation treatment of the driven electron-nuclear system, accounting for electron dephasing, where the nuclear system is reduced to collective states with polarization close to I_0 (*23*). **(C)** On the right, the ladder of electronic and nuclear states showing the carrier $I_z \rightarrow I_z$ and sideband transitions $I_z \rightarrow I_z \pm 1, I_z \pm 2$ from an initially spin-up polarized electron at a nuclear polarization of I_z. On the left, the same transitions represented within a single nuclear spin-$3/2$ manifold. **(D)** Spectra with optimal (violet) and poor (red) Raman cooling at average delay $\tau = 0 - 150$ ns. The dashed curves are Gaussian fits with standard deviation 7.7 MHz and 44.6 MHz, respectively. **(E)** Experimental spectrum buildup with $\Omega = 3.8$ MHz. **(F)** Spectrum at integrated delay $\tau = 850 - 1000$ ns. The solid curve is the same time slice averaged from the theory spectrum of panel B. The dashed curve is five Gaussian functions centered at $\delta \sim 0, \pm\omega_n, \pm 2\omega_n$ (*23*).

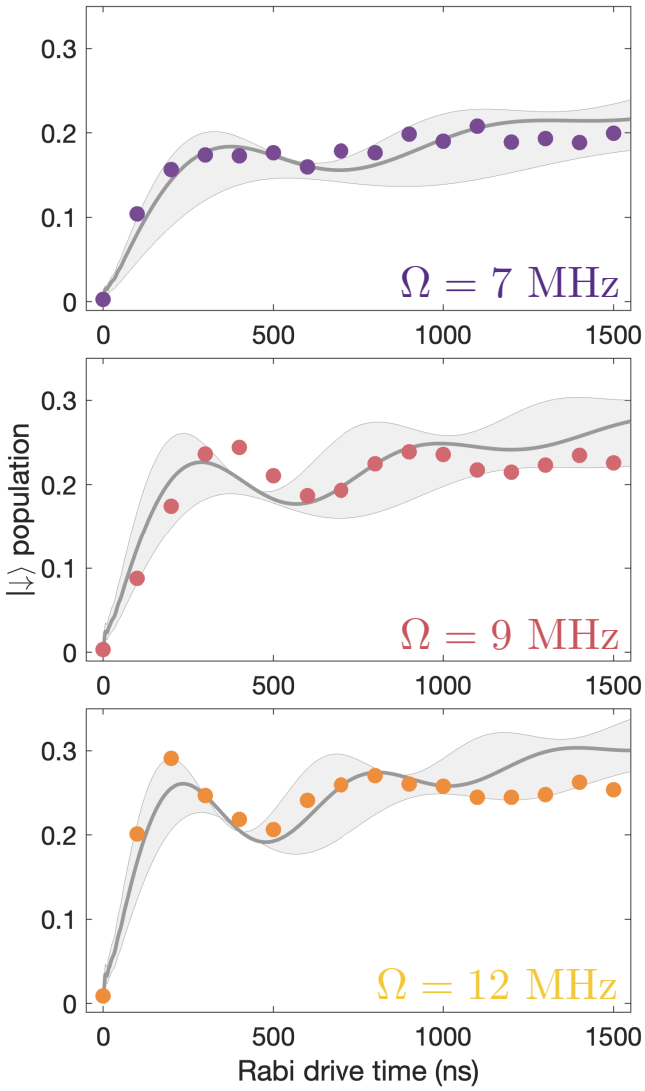

Figure 4: **Coherent oscillations of a nuclear magnon** Electronic excited-state $|\downarrow\rangle$ population (*23*), measured after a Rabi pulse of τ at $\delta = -2\omega_{\mathrm{n}} = -52$ MHz detuning, at 3.5 T. The carrier Rabi frequency Ω is 7, 9, and 12 MHz (*23*) for measurements shown in the top, middle, and bottom panels, respectively. Solid curves are the corresponding theoretical calculations with $\eta = 15\%$, using the same carrier Rabi frequencies. The shaded areas represent a $\sim \pm 20\%$ deviation in model Rabi frequency.

Supplementary Information for Quantum interface of an electron and a nuclear ensemble

D. A. Gangloff,[1*†] G. Éthier-Majcher,[1*‡] C. Lang,[1] E. V. Denning,[1,2] J. H. Bodey,[1] D. M. Jackson,[1] E. Clarke,[3] M. Hugues,[4] C. Le Gall,[1] M. Atatüre[1†]

[1]Cavendish Laboratory, University of Cambridge,
JJ Thomson Avenue, Cambridge CB3 0HE, United Kingdom
[2]Department of Photonics Engineering, Technical University of Denmark,
2800 Kgs. Lyngby, Denmark
[3]EPSRC National Epitaxy Facility, University of Sheffield,
Broad Lane, Sheffield, S4 7HQ, United Kingdom
[4]Université Côte d'Azur, CNRS, CRHEA,
rue Bernard Gregory, 06560 Valbonne, France

[*]These authors contributed equally to this work
[†]To whom correspondence should be addressed: dag50@cam.ac.uk, ma424@cam.ac.uk.

[‡] Present address: Anyon Systems Inc., 1985 55e Avenue #100, Dorval, QC H9P 1G9, Canada

Contents

1 Experimental System

1.1 Experimental schematic

A schematic of the experiment is shown in Fig. S1. The QD device is placed in a bath cryostat at 4K. A magnetic field is applied transverse to the QD growth axis (Voigt geometry). Two laser systems are combined and sent to the QD: a microwave-modulated Raman laser system (see section 1.3) and a resonant readout laser (Newport NF laser). A cross-polarisation confocal microscope followed by a grating setup is used for excitation and low-background fluorescence collection.

1.2 QD Device

Our QD device is from the same wafer as QD devices used in the group's previous work (*21, 30*). Self-assembled InGaAs QDs are grown by Molecular Beam Epitaxy (MBE) and integrated inside a Schottky diode structure (*16*), above a distributed Bragg reflector to maximize photon outcoupling efficiency. There is a 35-nm tunnel barrier between the n-doped layer and the QDs, and a tunnel barrier above the QD layer to prevent charge leakage. The Schottky diode structure is electrically contacted through Ohmic AuGeNi contacts to the n-doped layer and a semitransparent Ti gate (6 nm) is evaporated onto the surface of the sample. The photon collection is enhanced by placement of a superhemispherical cubic zirconia solid immersion lens (SIL) on the top Schottky contact of the sample. We estimate a photon outcoupling efficiency of 10% for QDs with an emission wavelength around 950 nm.

1.3 Raman laser system

The Raman laser source is a TOPTICA TA Pro. Raman beams are generated by modulating a fiber-based EOSPACE electro-optic amplitude modulator (EOM) with two switchable microwave tones. A Rohde & Schwartz 22GHz microwave

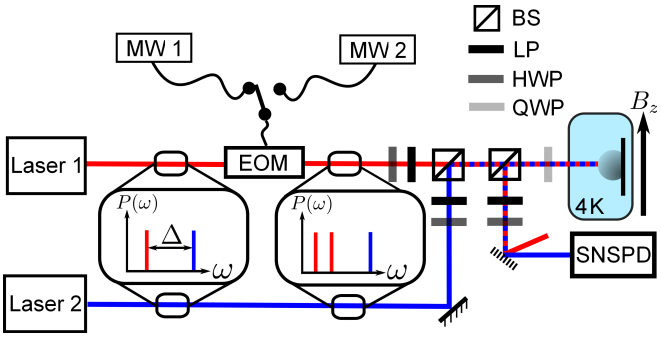

Figure S1: **Schematic of the experimental system.** We address the QD using two lasers. The first is intensity-modulated using an amplitude EOM driven by a microwave source (MW). We switch between two sources in order to drive the ESR at a two-photon detuning δ after first cooling the ensemble at $\delta = 0$. The second laser is resonant with a trion transition. Confocal microscopy is used to probe the QD with the lasers on separate input ports. To suppress background each is polarized orthogonally to the output port using half-wave plates (HWP) and linear polarizers (LP). The beams are combined on a beamsplitter before a quarter-wave plate (QWP) sets the polarization at the QD. The output is spectrally filtered with a diffraction grating to isolate the QD fluorescence, which we detect using a superconducting nanowire single-photon detector (SNSPD).

frequency source is frequency mixed with two outputs of a Tektronix Arbitrary waveform generator switched by a Mini-Circuits RF Switch. The mixer output is amplified to a peak power of 25 dBm. The Raman beams, with a combined optical power of $\sim$1 mW at the entrance to the cryostat, are passed through a quarter-wave plate and arrive at the quantum dot with near circular polarization at a red single-photon detuning $\Delta \gtrsim 2$ nm. The first-order EOM sidebands are two coherent laser fields whose energy difference can be made resonant with the electron spin resonance, as per this work $13-38$ GHz (corresponding to an applied magnetic field $B = 2-6$ T), leading to a two-photon detuning $\delta \approx 0$.

2 Measurements of the Overhauser field

2.1 Fluctuation measurements via electron spin coherence, T_2^*

The electron coherence function $C(\tau)$ is measured by performing Ramsey interferometry on the electron spin (*29, 30*). To do so, we make use of a mode-locked Coherent MIRA ps-pulsed laser detuned from the trion state resonance by $\sim$2 nm to perform ultrafast $\pi/2$ rotations of the electron spin (*37, 38*), separated by a time delay τ, followed by a spin-selective resonant readout, as shown in Fig. S3a. The visibility of the Ramsey fringes as a function of delay time τ (Fig. S3b) is captured by the coherence function $C(\tau)$ (Fig. S3c). The envelope of $C(\tau)$ is related by a simple Fourier transform to the Overhauser shift probability distribution $p(2A_cI_z)$ (Fig. S3d) (*39*), whose variance $4A_c^2\langle\Delta I_z^2\rangle = 2/T_2^{*2}$ is our measure of the effective nuclear ensemble temperature:

$$C(\tau) = \left| \int_{-\infty}^{\infty} p(2A_cI_z) \exp\left(-i2A_cI_z\tau\right) d(2A_cI_z) \right|$$

An extension of T_2^{*2} is therefore equivalent to narrowing the Overhauser shift probability distribution (*17–21, 39–43*).

2.2 Estimate of nuclear polarisation

We estimate the nuclear polarisation I_0 during our experiments by measuring the electron spin precession frequency following Raman preparation (see section 2.1), and comparing it to its thermal value in the absence of Raman preparation or dynamic nuclear polarisation effects altogether. It is possible to eliminate the buildup of nuclear polarisation across Ramsey measurement cycles by judiciously alternated initialisations of the electron spin, as in (*30*). At a magnetic field of 4T, the electron spin precession frequency is measured to be 25.221 ± 0.005GHz in the absence of preparation. It is measured to be 25.390 ± 0.005GHz in the presence of Raman preparation, as shown in Fig. S2b, which matches the Raman two-photon detuning that we control directly via the microwave source frequency (Fig. S1). In all our experiments, at all field values, we set this microwave frequency to be within $\pm$200 MHz of the expected zero-polarisation electron-spin resonance. This is where we reliably find the Raman resonance; the exact value within this frequency range does not affect the stability of the Raman resonance condition. Using our fitted value for the hyperfine constant $A_c = 600kHz$ (see section 10), we can convert this small detuning $\delta \leq 200$ MHz to a polarisation: $|I_0| \leq \delta/2A_c = 330$. This corresponds to a fractional polarisation of at most 0.7% in a pure spin-3/2 system, with an uncertainty of approximately 10 nuclear spins or 0.02% measured by Overhauser fluctuations of the cooled ensemble.

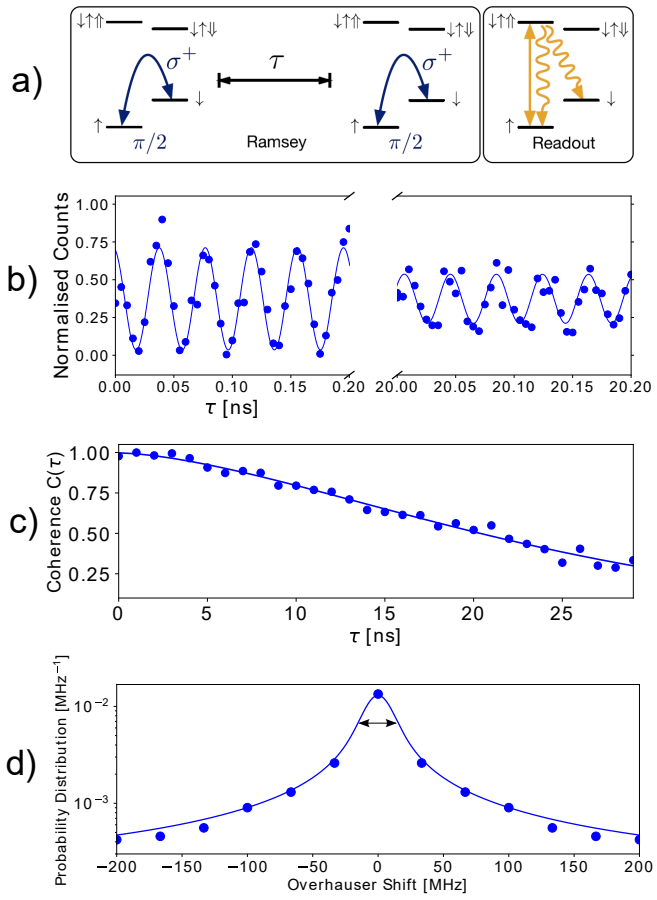

Figure S2: **Measuring nuclear spin fluctuations.** Data is taken at a magnetic field of 4 T. **(a)** Ramsey interferometry experimental sequence. **(b)** Normalized readout fluorescence as a function of Ramsey delay τ. The solid curves are sinusoidal fits. **(c)** Coherence function $C(\tau)$ defined as the visibility of the sinusoidal fit to the readout data in (b). The solid curve is a stretched exponential function $\exp(-(\tau/T_2^*)^\alpha)$, with fitted parameters $T_2^* = 26 \pm 7$ ns and $\alpha = 1.6 \pm 0.2$. **(d)** Probability distribution of the Overhauser shift, obtained from the Fourier transform of the coherence function $C(\tau)$.

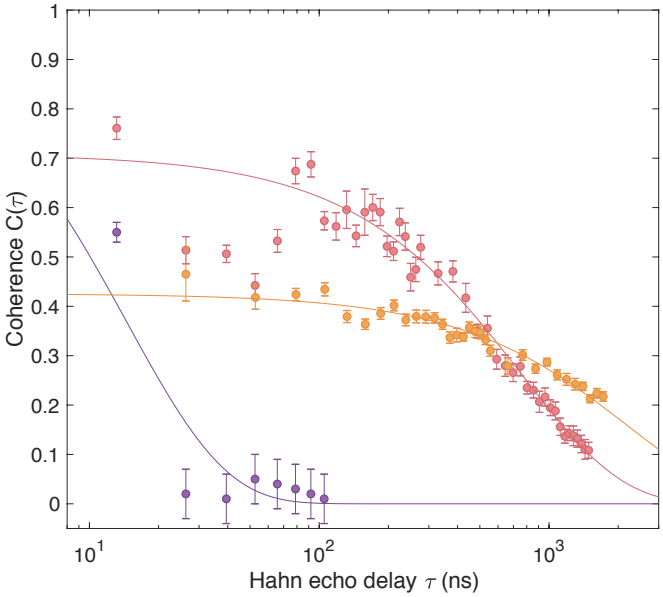

Figure S3: **Hahn Echo T_2 measurements** Measurement of the electron coherence as a function of the Hahn echo delay τ (time between two Ramsey $\pi/2$ pulses, with a π pulse inserted at $\tau/2$) at magnetic fields of 2 T (purple), 3 T (red), and 5 T (orange). The data are fitted with a simple exponential model $A\exp(-t/T_2)$, with the following fitted T_2 values: 15 ± 10 ns (2 T), 765 ± 15 ns (3 T), 2220 ± 70 ns (5 T).

3 Electron Hahn Echo T_2

The homogeneous dephasing time of the electron T_2 sets an important limit on cooling at low fields (Fig. 2e main text), and is one limit for coherent electron-nuclear exchange at the optimal field (Fig. 4 main text). Dephasing is dominated by high-frequency noise near the nuclear Zeeman frequencies arising from the hyperfine coupling of the electron to the nuclei, whose Zeeman eigenstates are mixed by quadrupolar interactions (*29, 30*). In Fig. S3, we present measurements of the Hahn Echo T_2 (*44*) measured at magnetic fields of 2 T, 3 T, and 5 T. These measured values are those used in our Raman cooling theory of Fig. 2 (main text) as well as the theory spectrum of Fig. 3 (main text).

4 Notes on nuclear system inhomogeneities

4.1 Electronic wavefunction and the hyperfine interaction

A gaussian-shaped electronic wavefunction simply means that a magnon excitation is not symmetrically distributed among the partaking spins. From the perspective of the electron, the magnon field has an amplitude resulting from a weighted sum of contributions from each nuclear spin according to its coupling strength to the electron.

In the absence of quadrupolar effects, the dominant dephasing mechanism on the magnon would be the Knight shift inhomogeneity; each spin evolving at a slightly different rate under the perturbed nuclear Zeeman hamiltonian. This contribution on the order of $A_c = 600$ kHz (section 10) is smaller than the optimal sideband coupling rate $\eta\Omega = 1.5$ MHz.

4.2 Strain dispersion and the quadrupolar interaction

An important source of inhomogeneity is that of the quadrupolar shift on the Zeeman splitting of the nuclei, owing to strain dispersion (described in more detail in section 5). The extent of this inhomogeneous broadening is fitted to be 3.9 MHz (section 5) in the spectrum of Fig. 3. This source of inhomogeneity is overcome at low-driving times owing to the fact that the subset of nuclei which couple more strongly to the electron (and have a correspondingly larger quadrupolar shift) will partake first in the magnon mode. The inhomogeneity of this subset is smaller than that of the full As ensemble, and therefore coherent coupling of $\eta\Omega = 1.5$ MHz is sufficient to observe a coherent interaction, as in Fig. 4.

4.3 Multiple nuclear species

In regards to cooling (Fig. 2), we expect that all three species, As, In, and Ga, are engaged in nuclear spin-flip processes that change the ensemble polarization I_z, and that the fluctuations ΔI_z^2 arising from all three species are reduced by cooling, albeit perhaps unequally. Nonetheless, for overall simplicity and to reduce the number of free parameters in our models, we make a single-species approximation under which As nuclei dominate the dynamics. This is justified in several ways:

- the quadrupolar angle of As makes it the species with the largest A_{nc} value (*45*)
- As has the lowest Zeeman energy, which makes its sideband coupling value of $\eta \propto \omega_{\text{n}}^{-2}$ the largest
- In the case of cooling, absorption on the first sideband $I_z \pm 1$ of the species with the lowest Zeeman energy is the first transition to become resonant for a deviation away from the steady-state.

As a result, the magnon modes observed in Fig. 3 and Fig. 4 are thought to be dominated by As nuclei. In our models presented alongside our data in both figures, we fix the nuclear Zeeman splitting to be that of As (as supported by a phenomenological five-gaussian fit of the spectrum in Fig. 3f), and fit two free quadrupolar interaction parameters (section 5). These are consistent with known As parameters for the quadrupolar constant $B_Q = 1.7$ MHz and quadrupolar angle $\theta = 20°$. These parameters suggest that As indeed exhibits the strongest sideband coupling strength η.

In a system where one species dominates, it is possible to address that species selectively: the buildup of electronic population due to resonant sideband excitation will be significantly faster for the dominant species and there exists as a result an initial window of driving times for which the spectrum is determined only by the dominant species. Hence our clearly resolved sidebands in Fig. 3. We are simply utilising the strength of coupling as an element of selectivity.

5 Microscopic origins of the sideband transitions

This section describes the perturbed hyperfine interaction that is the microscopic origin of the nuclear spin-flip sideband transitions.

The full Hamiltonian of the Raman-driven system with the Voigt B-field taken along the z-axis is (in a frame rotating with the Raman lasers and with the trion adiabatically eliminated)

$$H = \delta S_\mathrm{z} + 2\Omega S_\mathrm{x} + \sum_j \omega_\mathrm{n} I_\mathrm{z}^j - \sum_j 2A_\mathrm{c} I_\mathrm{z}^j S_\mathrm{z} + H_\mathrm{Q},$$

where we have ignored the flip-flop terms in the hyperfine interaction and H_Q describes the nuclear quadrupolar interaction (*26*),

$$H_\mathrm{Q} = \sum_j B_\mathrm{Q}\Big[I_\mathrm{x}^{j2}\cos^2\theta + I_\mathrm{z}^{j2}\sin^2\theta + (I_\mathrm{x}^j I_\mathrm{z}^j + I_\mathrm{z}^j I_\mathrm{x}^j)\frac{\sin 2\theta}{2}\Big],$$

where θ is the angle between the z-axis and the quadrupolar axis. Since the nuclear Zeeman splitting is much larger than the quadrupolar interaction strength, B_Q, the terms in H_Q that do not commute with I_z describe processes that are not allowed to first order. First, we extract the I_z-preserving and non-preserving parts of H_Q, which we denote by H_Q^0 and V_Q,

$$H_\mathrm{Q}^0 = \sum_j B_\mathrm{Q}[I_\mathrm{z}^{j2}\sin^2\theta + \frac{1}{2}(I_\mathrm{x}^{j2} + I_\mathrm{y}^{j2})\cos^2\theta]$$

$$V_\mathrm{Q} = \frac{1}{2}\sum_j B_\mathrm{Q}[(I_\mathrm{x}^{j2} - I_\mathrm{y}^{j2})\cos^2\theta + (I_\mathrm{x}^j I_\mathrm{z}^j + I_\mathrm{z}^j I_\mathrm{x}^j)\sin 2\theta].$$

The I_z-commuting part, H_Q^0, induces an anharmonic shift of the single-nucleus spin ladder of $\Delta_\mathrm{Q} = B_\mathrm{Q}(2\sin^2\theta - \cos^2\theta)$, whereas V_Q couples the nuclear Zeeman states. To obtain an effective Hamiltonian for the allowed low-energy excitations, we dress H with V_Q using a Schrieffer-Wolff transformation (*46, 47*). This removes V_Q and instead leads to a second-order correction term in the hyperfine interaction,

$$V_\mathrm{Q}' = S_\mathrm{z}\sum_j A_\mathrm{nc}\Big[(I_\mathrm{x}^{j2} - I_\mathrm{y}^{j2})\cos^2\theta + (I_\mathrm{x}^j I_\mathrm{z}^j + I_\mathrm{z}^j I_\mathrm{x}^j)\sin 2\theta\Big],$$

where $A_\mathrm{nc} = A_\mathrm{c}B_\mathrm{Q}/\omega_\mathrm{n}$, describing an effective non-collinear electron–nucleus interaction. This correction term, however, also describes a first-order energetically forbidden nuclear transition. Dressing the Hamiltonian with V_Q' replaces it by a correction to the electronic driving term,

$$V_\mathrm{Q}'' = -2\Omega S_\mathrm{y}\sum_j \frac{A_\mathrm{nc}}{\omega_\mathrm{n}}\Big[\frac{1}{2}(I_\mathrm{x}^j I_\mathrm{y}^j + I_\mathrm{y}^j I_\mathrm{x}^j)\cos^2\theta + (I_\mathrm{z}^j I_\mathrm{y}^j + I_\mathrm{y}^j I_\mathrm{z}^j)\sin 2\theta\Big],$$

which describes higher-order simultaneous nuclear–electron transitions induced by the Raman drive.

To evaluate the strength of sideband transitions, we evaluate matrix elements of V_Q'' with respect to the collective nuclear I_z-eigenstates, $|I_\mathrm{z}\rangle$, we find the matrix elements

$$\langle I_\mathrm{z}'|V_\mathrm{Q}''|I_\mathrm{z}\rangle = -2S_\mathrm{y}\frac{\Omega A_\mathrm{nc}}{\omega_\mathrm{n}}\mathcal{D}_{I_\mathrm{z},I_\mathrm{z}'}\Big\{\sin 2\theta\big[\delta_{I_\mathrm{z}',I_\mathrm{z}+1} + \delta_{I_\mathrm{z}',I_\mathrm{z}-1}\big] + \frac{\cos^2\theta}{2}\big[\delta_{I_\mathrm{z}',I_\mathrm{z}+2} + \delta_{I_\mathrm{z}',I_\mathrm{z}-2}\big]\Big\}, \tag{1}$$

where $\mathcal{D}_{I_\mathrm{z},I_\mathrm{z}'}$ is an enhancement factor accounting for the degeneracy of the transition. The terms in Eq. (1) proportional to $\sin 2\theta$ describe the $\Delta I_z = \pm 1$ sideband transitions, and the terms proportional to $\cos^2\theta$ describe the $\Delta I_z = \pm 2$ transitions. Assuming that the nuclear bath is unpolarized and thus $I_\mathrm{z}, I_\mathrm{z}' \simeq 0$, we find for spin-3/2 nuclei

$$\big|\mathcal{D}_{I_\mathrm{z},I_\mathrm{z}'}\big| \simeq \sqrt{3N/4}. \tag{2}$$

5.1 Theory for sideband spectrum

To model the excitation spectrum of the electron spin in the presence of the nuclear sideband transitions, we assume that the initial nuclear density operator can be written as a classical mixture of $|I_\mathrm{z}\rangle$-states described by the cooled Overhauser distribution, $p(I_\mathrm{z})$. In each realisation of the ensemble, $|I_\mathrm{z}\rangle$, we expand the nuclear state on the relevant five-dimensional subspace $\{|I_\mathrm{z}\rangle, |I_\mathrm{z}\pm 1\rangle, |I_\mathrm{z}\pm 2\rangle\}$ and calculate the dynamics under the approximation (2) using the master equation for the combined electron-nuclear system,

$$\frac{\partial\rho(t|I_z)}{\partial t} = i[\rho(t|I_\mathrm{z}), H] + \sum_{I_\mathrm{z}'=I_\mathrm{z}-2}^{I_\mathrm{z}+2}\Gamma_\mathrm{n} L(|I_\mathrm{z}'\rangle\langle I_\mathrm{z}'|) + \frac{1}{T_2}L(S_\mathrm{z}), \tag{3}$$

where $\rho(t|I_\mathrm{z})$ is the density operator conditional on the initial nuclear state being I_z, $L(a) = a\rho(t|I_\mathrm{z})a^\dagger - \frac{1}{2}\{a^\dagger a, \rho(t|I_\mathrm{z})\}$ is the Lindblad operator, and Γ_n is broadening of the collective nuclear states due to quadrupolar fine structure, $\Gamma_\mathrm{n} = 2(1+\alpha)|\Delta_\mathrm{Q}|$. Here, α is the relative variation of Δ_Q in the nuclear ensemble due to inhomogeneous strain, which is estimated to be $\sim 80\%$, based on (*45*). The last term in (3) accounts for electronic dephasing induced by nuclear diffusion. The ensemble density operator, χ, is then calculated

by averaging the conditional density operator $\rho(t|I_z)$ over the different initial configurations $\chi(t) = \int \mathrm{d}I_z\, p(I_z)\rho(t|I_z)$.

Fig. 3b (main text) shows the theoretically predicted excitation map resulting from the master equation, (3). The quadrupolar parameters are fitted to the experiment (Fig. 3e main text), from which we obtain: $B_\mathrm{Q} = 1.7\,\mathrm{MHz},\ \theta = 20.4^\circ$. These fitted values are consistent with parameters for As nuclei from literature (*45*). Other parameters are taken from the experimental configuration, $\omega_\mathrm{n}/2\pi = 7.22\,\mathrm{MHz/T}, B = 3\,\mathrm{T}, \Omega/2\pi = 3.3\,\mathrm{MHz},\ T_2 = 1.5\,\mu\mathrm{s}$.

In relation to the sideband strength relative to the carrier Rabi frequency, η, these parameters yield the first sideband strength $\eta_1 = (A_\mathrm{nc}/\omega_\mathrm{n})(\sqrt{3N/4})(\sin 2\theta) = 0.1$ and the second sideband strength $\eta_2 = (A_\mathrm{nc}/\omega_\mathrm{n})(\sqrt{3N/4})(\cos^2\theta/2) = 0.14$.

6 More details on fitting the electron resonance spectrum

The spectrum in Fig. 3f (main text) is fitted with a sum of five Gaussian functions $\mathcal{G}(A, \delta, \sigma)$ of amplitude A (population), detuning δ (MHz), and standard deviation σ (MHz), appearing as a dashed line that agrees closely with the data. The result of the fit is: $\mathcal{G}(0.40(1), 0.0(2), 7.5(3)) + \mathcal{G}(0.27(1), 22.0(3), 7.2(4)) + \mathcal{G}(0.27(1), -22.6(3), 7.1(4)) + \mathcal{G}(0.10(1), 46.3(9), 9.6(9)) + \mathcal{G}(0.13(1), -47.8(9), 11.9(9))$.

7 Raman cooling

7.1 Cooling model

7.1.1 Two-level limit

We consider two fields with orthogonal polarization driving a three-level system: a V-polarized field driving the V-polarized exciton transition $|\uparrow\rangle$ to the trion state $|\Uparrow\uparrow\downarrow\rangle$ with resonant Rabi frequency Ω_V and detuning Δ_V, and an H-polarized field driving the H-polarized exciton transition $|\downarrow\rangle$ to the same trion state $|\Uparrow\uparrow\downarrow\rangle$ with resonant Rabi frequency Ω_H and detuning Δ_H. In the limit where these fields do not populate the trion excited state, $\Omega^2_\mathrm{H,V}/\Delta^2_\mathrm{H,V} \ll 1$, we can ignore the excited state contribution and reduce the driven three-level system to a driven two-level system split by the electron Zeeman energy ω_e, where the two-photon transition between the electronic states $|\uparrow\rangle$ and $|\downarrow\rangle$ has a resonant Rabi frequency $\Omega = \Omega_\mathrm{H}\Omega_\mathrm{V}/2\Delta$, $\Delta = (\Delta_\mathrm{H} + \Delta_\mathrm{V})/2$, and a detuning from electron spin resonance of $\delta = \Delta_\mathrm{V} - \Delta_\mathrm{H} - \omega_\mathrm{e}$.

In the presence of an additional field with resonant Rabi frequency Ω_p performing resonant optical pumping on the H-polarized transition, the $|\downarrow\rangle$ state acquires an effective linewidth that is the inverse of its lifetime under optical pumping:

$$\Gamma = \frac{\Gamma_0}{4}\frac{2\left(\Omega_\mathrm{p}/\Gamma_0\right)^2}{1 + 2\left(\Omega_\mathrm{p}/\Gamma_0\right)^2},$$

where $\Gamma_0 \approx 150$ MHz, is the natural linewidth of the trion excited state. The optical pumping field Rabi frequency Ω_p can thus be used to tune the excited state linewidth of the two-level system in the range $[0, \Gamma_0/4]$.

We can hereon treat scattering in the two-level system as per the textbook formula, given a driving field with Rabi frequency Ω, excited state with linewidth Γ, and dephasing rate Γ_2. In relation to the main text, this gives then the stimulated Raman scattering rate on the central electron spin transition at a detuning δ:

$$W(\delta) = \frac{\Gamma}{2}\frac{(\Omega^2/\Gamma\Gamma_2)}{1 + (\Omega^2/\Gamma\Gamma_2) + (\delta/\Gamma_2)^2},$$

7.1.2 Cooling

The sideband processes are best represented in a ladder of states, where we consider the electron spin states dressed by the nuclear states of polarization $I_\mathrm{z} = [-NI, NI]$ (for spin-I nuclei), as in Fig. 1 (main text). In this simple picture, V''_Q allows transitions which change nuclear spin polarization by one (or two) nuclear spin flip, in either direction. Towards cooling, which results in a polarization which deviates from its steady-state over an energy scale well below the nuclear Zeeman energy, we consider that the $I_z \pm 1$ sideband largely dominates the process, and its coupling strength is a fraction $\eta = (\sqrt{NI/2})(A_\mathrm{nc}/\omega_\mathrm{n})(\sin 2\theta)$ (for spin-I) of the coupling on the central transition.

Combining these sideband processes within our Raman-driven two-level system where one electron spin state relaxes to the other, we obtain two types of rates that change the nuclear spin polarization, drift rates $W_\pm$ arising from stimulated sideband transitions, and a diffusion rate Γ_nc arising from spontaneous sideband transitions, each occuring at a maximum rate of $\eta^2\Gamma/2$ with a spectral response function defined by the polarization-dependent Raman scattering rate $W(\delta, I_z)$:

$$W_\pm(\delta, I_z) = \eta^2\frac{\Gamma}{2}\frac{(\Omega^2/\Gamma\Gamma_2)}{1 + (\Omega^2/\Gamma\Gamma_2) + (\Delta_\pm(\delta, I_z)/\Gamma_2)^2}$$

$$\Gamma_\mathrm{nc}(\delta, I_z) = \eta^2\frac{\Gamma}{2}\frac{(\Omega^2/\Gamma\Gamma_2)}{1 + (\Omega^2/\Gamma\Gamma_2) + ((\delta - A_\mathrm{c}I_z)/\Gamma_2)^2}$$

Where the effective detuning $\Delta_\pm(\delta) = (\delta - A_\mathrm{c}(I_\mathrm{z} \pm 1) \mp \omega_\mathrm{n})$, and we take the dephasing rate $\Gamma_2 = (\Gamma/2 + 1/T_2)\sqrt{1 + 2\left(\Omega_\mathrm{p}/\Gamma_0\right)^2} + \Delta\omega_\mathrm{n}$ to be determined by the electronic excited state linewidth Γ, the homogeneous dephasing time of the electron spin resonance T_2, power broadened by the optical pumping saturation $2\left(\Omega_\mathrm{p}/\Gamma_0\right)^2$, and by the inhomogeneous broadening $\Delta\omega_\mathrm{n}$ of the nuclear Zeeman energies

arising primarily from the multiple nuclear species partaking in the process.

The equation above stands as the elementary description of dynamic nuclear polarisation (*6, 27, 48–50*). For a fixed two-photon detuning $\delta = 0$, the evolution of the nuclear polarization is given by:

$$\frac{dI_z}{dt} = W_+(I_z)(1 - \frac{I_z}{NI}) - W_-(I_z)(1 + \frac{I_z}{NI}) - \Gamma_d(I_z)\frac{I_z}{NI}$$

Where $\Gamma_{\mathrm{d}}(I_z) = \Gamma_{\mathrm{nc}}(I_z) + \Gamma_{\mathrm{em}}$ is the total diffusion term composed of a polarization-dependent optical diffusion Γ_{nc} as defined above, and a constant rate non-optical electron mediated diffusion term Γ_{em} which we report on in a later section of this supplementary.

We can re-arrange this rate equation:

$$\begin{aligned}\frac{dI_z}{dt} &= -\left(W_+(I_z) + W_-(I_z) + \Gamma_d(I_z)\right) \\ &\quad \left(\frac{I_z}{NI} - \frac{W_+(I_z) - W_-(I_z)}{W_+(I_z) + W_-(I_z) + \Gamma_d(I_z)}\right) \\ \frac{dI_z}{dt} &= -\frac{\Gamma_{\mathrm{tot}}}{NI}\left(I_z - NIs^{(1/2)}(I_z)\right),\end{aligned}$$

where, following Yang & Sham (*28*), we have defined $\Gamma_{\mathrm{tot}} = W_+(I_z) + W_-(I_z) + \Gamma_d(I_z)$, and have made the association that $s^{(1/2)}(I_z) = (W_+(I_z) - W_-(I_z))/\Gamma_{\mathrm{tot}}$ is the steady state fractional polarization for spin-$1/2$ nuclei. This acts then as proportional to the cooling function $f(I_z) = NIs^{(1/2)}(I_z)$ as per the formula in the main text. We make the approximation that the nuclear polarization is small, $|I_z| \ll N$, which is where we conduct our experiments, and as such we can approximate the steady-state nuclear polarization for an arbitrary spin-I as:

$$s(I_z) \approx \frac{2}{3}(I+1)\frac{W_+(I_z) - W_-(I_z)}{W_+(I_z) + W_-(I_z) + \Gamma_d(I_z)}$$

Steady-state is then simply obtained by the numerically solvable self-consistent equation:

$$s(I_0) = I_0/NI$$

We note here that the gradient $f'(I_0)$, which we relate to the damping coefficient, depends intimately on the relationship between ω_{n}, A_{c}, and Γ through the spectral function $\Delta_\pm/\Gamma_2$. Two competing demands exists on Γ. First, the simple condition that some sideband scattering is required near the stable point I_0 in order for good Raman cooling to occur means that the Raman rate Ω and linewidth Γ must be comparable to the nuclear Zeeman energy ω_{n}; this means making $\Gamma/\omega_{\mathrm{n}} \approx 1$. Secondly, the spectral selectivity over the Overhauser shift $2A_{\mathrm{c}}I_z$, which improves narrowing around a given value of I_z, depends on the ratio A_{c}/Γ, which needs to be large for good cooling. These two competing effects lead to an optimal value of Γ, which is ultimately determined by just how much scattering is needed near the stable point I_0 to beat non-optical diffusion Γ_{em}.

Linearising $f(I_z)$ around the stable point I_0, it is possible to obtain the steady-state distribution $p(I_z)$ under a Fokker-Planck treatment of the diffusion equation, and to obtain an analytical expression for the steady-state reduction in the width of the thermal distribution $\Delta I^2_{\mathrm{z,th}}$:

$$\frac{\Delta I_{\mathrm{z}}^2}{\Delta I^2_{\mathrm{z,th}}} = \frac{1 - \left(\frac{3}{2(I+1)}\frac{I_0}{NI}\right)^2}{1 - \frac{2(I+1)}{3}f'(I_0)}$$

Hence, it is clear that for any reduction of fluctuations around I_0, we require $|f'(I_0)| > 0$. The above analytical result forms the basis for our theoretical cooling predictions in Fig. 2 (main text). In our measurements we obtain the ratio $\Delta I_{\mathrm{z}}^2/\Delta I^2_{\mathrm{z,th}}$ by exploiting the straightforward relationship between ΔI_{z}^2 and T_2^* (obtained from Ramsey measurement of the electron spin splitting):

$$\frac{\Delta I_{\mathrm{z}}^2}{\Delta I^2_{\mathrm{z,th}}} = \left(\frac{T^*_{2,\mathrm{th}}}{T_2^*}\right)^2$$

7.2 Further measurements

7.2.1 Cooling measurements at 3 T and 6 T

In Fig. 2a (main text), we reported our cooling performance measurements as a function of both Raman rate and excited state linewidth performed at a magnetic field of 5 T. The same measurements were performed at 3 T and 6 T, which we show here in Fig. S4. The optimal cooling performance and the corresponding Raman rate and linewidth are those reported in Fig. 2d,e (main text).

7.2.2 Note on measurement at 4 T

At 4 T, we only varied the excited state linewidth Γ near the interpolated optimal value of Ω, which gives a good approximation of the optimal excited state linewidth within our measurement error. As a result we present in Fig. 2d (main text) an optimal excited state value but not an optimal Raman rate at this magnetic field.

7.2.3 Nuclear spin diffusion: relaxation of the probability distribution variance

In the absence of cooling ($W_\pm = 0$), the nuclear spin distribution relaxes back to its equilibrium distribution giving us information on the non-optical nuclear spin diffusion rate Γ_{em} that plays an important role in limiting the cooling efficiency at all fields. In Fig. S5, we show a measurement performed at 3 T of the nuclear polarization fluctuations ΔI_{z}^2, normalized by their thermal value $5N/4$, as they relax from their cold nonequilibrium steady-state to their thermal state in the absence of cooling, as a function of delay time between cooling and Ramsey measurement of the fluctuations (*21*).

The relaxation is fitted well by an exponential model for which the asymptotic behaviour is fixed $4\Delta I_z^2/5N \rightarrow 1$, as we know from measuring the electron coherence at thermal equilibrium (*21*). The typical relaxation time of the fluctuations $\tau = 41.7 \pm 1.2$ms is used as the model parameter $1/\Gamma_{\rm em}$ which is part of the nuclear depolarization rate Γ_d that is used in our theoretical calculations presented in Fig. 2 (main text). This mechanism is only present when an electron is present in the QD, which points towards an electron-mediated mechanism (*21, 31, 32*). In this respect, the diffusion rate ought to be inversely proportional to the electron spin splitting squared $\Gamma_{\rm em}(B) \propto B^{-2}$, where $\Gamma_{\rm em}(3) = 1/\tau$, and this is the scaling we use to obtain our theory curves in Fig. 2 (main text).

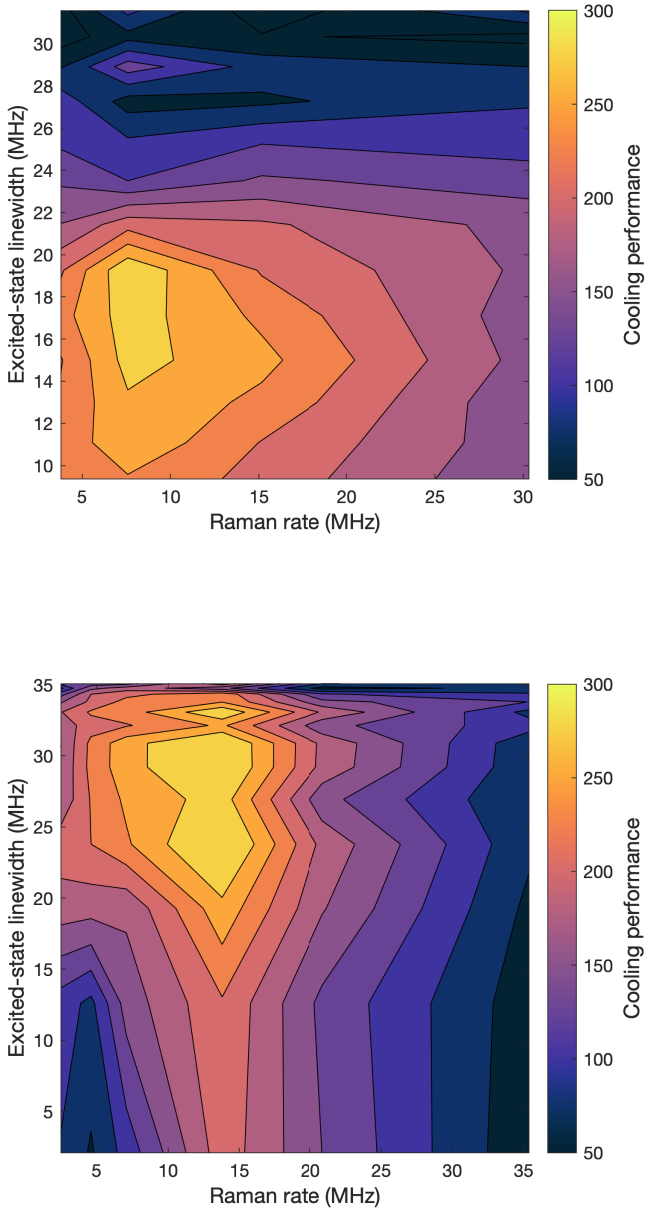

Figure S4: **Raman cooling at 3T and 6T (a)** Experimental map of the cooling performance as a function of Raman rate and excited state linewidth at a magnetic field of 3T **(b)** The same at a magnetic field of 6T.

7.3 Additional notes on global limit to cooling performance

Even in the absence of non-optical nuclear spin diffusion mechanisms ($\Gamma_{\rm em} = 0$, $\Gamma_{\rm d} = \Gamma_{\rm nc}$), the simple condition that some sideband scattering is required close to the steady state polarization I_0 in order to maintain Raman cooling, i.e. $|f'(I_0)| > 0$, means that the Raman rate Ω and linewidth Γ must be of the order of the nuclear Zeeman energy $\omega_{\rm n}$. The dependence of sideband absorption rate on the polarization $I_{\rm z}$ is a function of the Overhauser shift $2A_{\rm c}I_{\rm z}$, and as a result the damping coefficient $f'(I_0)$ depends on the ratio of the Overhauser shift to the Zeeman energy $A_{\rm c}/\omega_{\rm n}$. This condition thus entails a limit on the spectral selectivity that is intrinsic to the sideband cooling mechanism we employ: the larger the energy splittings at play, the less efficient the cooling. As a result, the cooling efficiency is inversely proportional to the magnetic field. The resulting field-dependence is shown as a dotted theory line in Fig. 2e (main text) bounding the red shaded region.

The field-dependence of the cooling efficiency is accentuated by an explicit dependence of the sideband scattering on magnetic field, i.e. $W_{\pm} \propto \eta^2 \propto \omega_{\rm n}^{-4}$. The electron-mediated nuclear spin diffusion mechanism (*31, 32*) plays a significant role in our system as described in the previous section. This

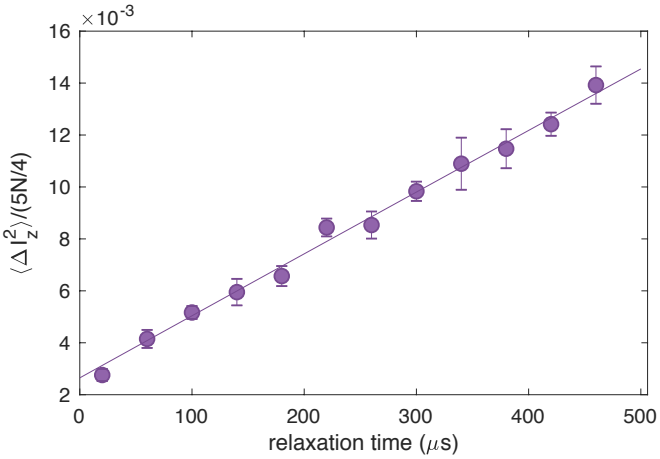

Figure S5: **Relaxation of the nuclear spin fluctuations** Measurement at 3T of the nuclear polarization variance $\Delta I_{\rm z}^2$, normalized by its thermal value $5N/4$, as it relaxes from its cold state to its thermal state in the absence of cooling, as a function of delay (relaxation) time between cooling and Ramsey measurement of the fluctuations. The solid curve is a fit to the model $1 - a\exp(-t/\tau)$, for which we obtain $a = 0.9974 \pm 0.0003$ and $\tau = 41.7 \pm 1.2$ ms.

diffusion mechanism decreases the cooling performance at all fields. It has a field dependent rate $\propto B^{-2}$ and, when added to the sideband model, leads to a sharper decrease of cooling efficiency with increasing field, as seen from the high-field behavior of the solid theory line in Fig. 2e (main text).

Lastly, at magnetic fields below 2T, where the nuclear Zeeman eigenstates are strongly mixed by strain and the resulting fast precession of a wide spectrum of nuclear-spin frequencies dephase the electron spin over a time T_2 (*29, 30*), the Raman resonance is homogeneously broadened to a linewidth $\Delta\nu_{\mathrm{Q}} \sim 1/T_2 > 20$ MHz and thereby imposes that limit on the width of the nuclear spin distribution that can be prepared with Raman cooling. This leads to the dashed theory line in Fig. 2e (main text) bounding the blue shaded area.

We summarize our measurements under these cooling limits in Fig. 2e (main text), where it is clear that we reach our system's global temperature optimal at a magnetic field around 3.3T.

8 A relation to canonical temperature

We define the effective temperature of the nuclear spin ensemble as the temperature of a thermal ensemble that would feature the same polarization fluctuations ΔI_z^2 as those we measure. We make a number of assumptions to relate the measured system properties to a temperature:

- the energy of the system is characterized by I_{z} (i.e. we neglect the quadrupole shifts of the collective state)
- we neglect the presence of multiple nuclear isotopes and take the nuclear Zeeman energy of As (spin-$3/2$), which has the lowest Zeeman splitting, and therefore provides a lower bound on the temperature
- we consider that the average polarization I_z probed by the electron spin is representative of the nuclear polarization of the QD, which is only exactly true for homogeneous coupling

We define the partition function of the nuclear spin system expressed in the collective I_z basis, where we account for the degeneracy $g(I_z)$ of each state:

$$Z(\beta) = \sum_{I_z=-3N/2}^{3N/2} g(I_z)\exp(-\beta I_z),$$

where $\beta = \hbar\omega_{\mathrm{n}}/k_{\mathrm{B}}T$. The degeneracy term $g(I_z)$ is a sum of binomial coefficients corresponding to the number of ways a state I_z can be thermally occupied accounting for individual spin-$3/2$ structures that contain four internal states (*51*). As an example, for $I_z = -3N/2+2$ (i.e. two nuclear spin flips away from maximal polarization), this can occur with two separate spins increasing their internal energy by one unit, or a single spin increasing its internal energy by two units. Here we show this degeneracy factor in order of increasing unit jumps:

$$\begin{aligned}
g(-3N/2) &= 1 \\
g(-3N/2+1) &= \binom{N}{1} \\
g(-3N/2+2) &= \binom{N}{2} + \binom{N}{1} \\
g(-3N/2+3) &= \binom{N}{3} + \binom{N}{1}\binom{N-1}{1} \\
&\quad + \binom{N}{1} \\
&\quad \ldots
\end{aligned}$$

What we deduce from this sequence is that the term with single unit jumps (i.e. the first term) dominates the count by a factor $O(N)$ for high polarization $I_z \lesssim -N$ (for which this first term reaches a maximum), and thus serves as a good approximation when considering the low temperature regime $\beta > 1$. We thus approximate the partition function as:

$$Z(\beta) \approx \sum_{I_z=-3N/2}^{-N} \binom{N}{I_z + 3N/2} \exp(-\beta I_z),$$

where we have truncated the sum at $I_z = -N$, which yields a sufficient number of terms in the sum for a low temperature approximation. Note that this result is exact for spin-$1/2$ particles.

From the partition function $Z(\beta)$, it is then a simple matter to calculate the moments for a thermal distribution:

$$\langle I_z^k \rangle = \frac{(-1)^k}{Z(\beta)} \frac{\partial^k Z(\beta)}{\partial \beta^k}$$

and most importantly the variance ΔI_z^2:

$$\begin{aligned}
\Delta I_z^2 &= \langle I_z^2 \rangle - \langle I_z \rangle^2 \\
&= \frac{-1}{Z(\beta)} \frac{\partial^2 Z(\beta)}{\partial \beta^2} - \left(\frac{1}{Z(\beta)} \frac{\partial Z(\beta)}{\partial \beta} \right)^2
\end{aligned}$$

We can plot the mean polarization $|\langle I_z \rangle|$ and the fluctuations ΔI_z^2 as a function of β, shown in Fig. S6. From this plot, it becomes clear that any significant reduction of fluctuations $\Delta I_z^2 \ll N$ is accompanied by a reduction of temperature below the system's defining energy scale, i.e. the nuclear Zeeman splitting ω_{n}; this corresponds to $\beta > 1$. Our maximum measured cooling performance $(5N/4)/\Delta I_z^2 = 400$ can also be seen as the reduction of fluctuations to a level of $\Delta I_z^2 = (5N/4)/400 \approx 100$. From our theory curves in Fig. S6, this corresponds to a thermal ensemble with $\beta = 5.5$ and a polarization around 99.9%. There, the equivalent temperature is $T = (\hbar\omega_{\mathrm{n}}/k_{\mathrm{B}})/5.5 \approx 200\mu$K.

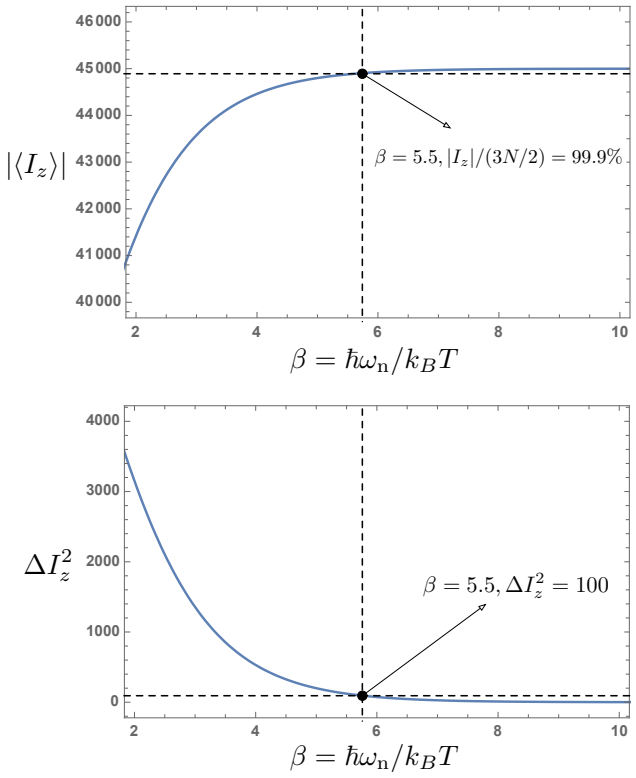

Figure S6: **Mean polarization and fluctuations as a function of inverse temperature.** Curves are calculated from a canonical ensemble of non-interacting spin-3/2 nuclei, in the collective polarization I_z basis, as a function of inverse temperature $\beta = \hbar\omega_n/k_B T$. Dashed lines mark values corresponding to our maximum measured cooling performance, $\Delta I_z^2 = (5N/4)/400 \approx 100$.

9 Nuclear magnon oscillations

9.1 Extracting η, carrier Rabi oscillations

The sideband parameter η is a model parameter representing the ratio of oscillation frequency on the sideband $\eta\Omega$ relative to the carrier Ω. In Fig. 4, we present sideband oscillations taken at $\delta = -52$ MHz from which we obtain $\eta = 15\%$. In Fig. S7, we present the corresponding carrier Rabi oscillations for the same drive strength $\Omega = 9$ MHz (middle panel of Fig. 4).

9.2 Nuclear magnon vs electron population

In Fig. 4, our theory curves showed what we measure in our experiment: the electron excited state population summed over all nuclear states. In our simulations, we can however readout the particular nuclear state $|I_z - 2\rangle$ that we target with our sideband drive. Here we show as Fig. S8 a version of Fig. 4 (main text), where the population of the target nuclear state is shown alongside the main theory curve and the data.

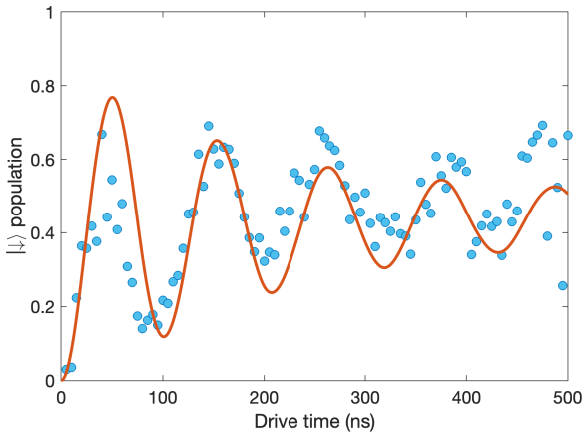

Figure S7: **Carrier Rabi oscillations.** Electronic $|\downarrow\rangle$ population, measured after a Rabi drive time, at a detuning $\delta \approx 0$, at 3.5T. The solid line is from a model with Rabi frequency $\Omega = 9$ MHz that accounts for the effects of Overhauser field fluctuations, of the inhomogeneous broadening of nuclear Zeeman energies, and of a small systematic detuning of $\delta = 3$MHz in our measurement.

Table S1: Summary of directly measured experimental parameters (single parameter fits)

Wavelength	950 nm
Electron $g_e\mu_B$	6.3 GHz/T
Inhomogeneous dephasing time $T^*_{2,th}$	1.7 ns
Homogeneous dephasing time T_2 (2 T)	20 ns
Homogeneous dephasing time T_2 (3 T)	500 ns
Homogeneous dephasing time T_2 (5 T)	2000 ns
Sideband coupling η at 3.5 T (Fig. 4)	0.15
Nuclear relaxation time $T_{1,n}$ (3 T)	42 ms

10 Summary of model values

Table S2: Summary of fitted model parameters (multi-parameter fits)

Number of nuclei N (Fig. 2)	3×10^4
Trion linewidth Γ_0 (Fig. 2)	150 MHz
A_c (Fig. 2)	600 kHz
Nuclear Zeeman spread $\Delta\omega_n$ at 3 T (Fig. 2)	10 MHz
η at 3 T (Fig. 2)	0.063
η_1 at 3 T (Fig. 3 1st sideband)	0.10
η_2 at 3 T (Fig. 3 2nd sideband)	0.14
Nuclear broadening Γ_n (Fig. 3)	3.9 MHz
Nuclear broadening Γ_n (Fig. 4)	0.7 MHz
Homogeneous dephasing time T_2 at 3.5 T(Fig. 4)	5000 ns

Our models contain a number of parameters whose range of values is well-known from previous studies (*16, 26, 30, 45*), but whose exact value is determined by fitting our data in sev-

eral independent experiments.

The cooling experiments of Fig. 2 (main text) are fitted with our single-species Raman cooling model described earlier in this SI. We fix the nuclear Zeeman splitting to be that of As, corresponding to a gyromagnetic ratio of 7.22 MHz/T, and the spin to $I = 3/2$. We introduce a nuclear Zeeman broadening free parameter $\Delta\omega_n$ representing the effective spread of Zeeman energies arising from the contribution of other species and from quadrupolar interactions, which acts as an inhomogeneous broadening term in the Raman scattering rate. The other free parameters of this model are the number of nuclei N, the collinear hyperfine constant A_c, the noncollinear hyperfine constant A_{nc}, and the trion excited state linewidth Γ_0. While these parameters are "free", we emphasize that they are tied to independently measured values, from both our own measurements and from literature, and are thus formally tied to specific ranges. $\Delta\omega_n$ should be no less than the Zeeman energy broadening of $\sim$ 3 MHz arising from strain inhomogeneities for a single species, and no more than these inhomogeneities added to the spread of species Zeeman energies, $\sim$ 30 MHz (at 3 T). The number of nuclei N should be in the range $10^4 - 10^6$ (*16*). The total Overhauser shift NIA_c should be no less than for GaAs 16.3 GHz, and no more than for InAs 38.1 GHz (*16*). The noncollinear hyperfine constant A_{nc}/A_c should be in the range $0.01 - 0.08$ based on previous measurements and calculations (*26, 45*). The trion state lifetime, known to be $\sim$1 ns (*16*), corresponds to linewidths $100 - 400$ MHz.

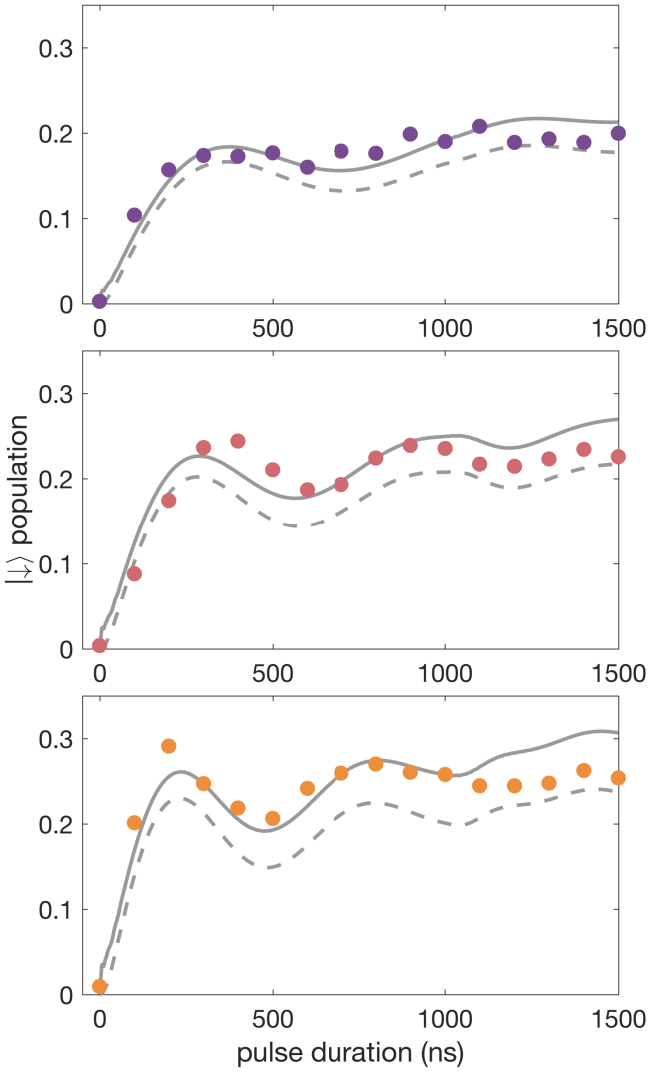

Figure S8: **Coherent electron-magnon exchange** Electronic excited state $|\downarrow\rangle$ population, measured after a Rabi pulse of τ at a detuning $\delta = -2\omega_n = -52$ MHz, for a magnetic field of 3.5 T, measured for carrier Rabi frequencies $\Omega = 7, 9, 12$ MHz (top to bottom). Solid curves are the corresponding theoretical calculations of identical carrier Rabi frequencies. The dashed curves are the simulated population transferred only to state $|\downarrow, I_z - 2\rangle$.

The collinear hyperfine interaction product $A_c\sqrt{N_t}$ is tied to the inhomogeneous dephasing time T_2^* of the electron (*29, 30*) in the absence of any cooling; $T_2^* = \left[(2/3)N_t\langle A_c^2 I(I+1)\rangle\right]^{-1/2}$. $\langle\rangle$ is the species-averaged value of individual nuclear spin I and hyperfine constant A_c, where we take the Indium concentration to be 50% as per previous measurements on quantum dots from the same wafer (*30*). Note that while not all species may contribute to the cooling equally, all species will contribute to the thermal fluctuations of the ensemble. As such, all N_t spins in the QD should be counted here. We measure $T_2^* = 1.7$ ns, which gives the product $A_c\sqrt{N_t} = 190$ MHz. The free parameter value of $A_c\sqrt{N}$ we arrive at from fitting our cooling data (Fig. 2 main text) with our model is 104 MHz. Within our model, N is the fitted number of spins that partake in the cooling process, which we know to be effectively smaller than the total number of spins of all species N_t. This discrepancy could be thus explained if indeed $N/N_t = 33\%$ of spins took part in the cooling.

The fitted values of the total Overhauser shift $NIA_c = 27$ GHz agrees well with an InGaAs QD with 50% In. The fitted non-collinear hyperfine constant $A_{nc}/A_c = 0.015$, and the number of spins 3×10^4 match those of previous studies on non-collinear feedback effects in InGaAs QDs (*26*).

The trion excited state linewidth, fitted to $\Gamma_0 = 150$ MHz, sets the absolute scale on the optical parameters Ω and Γ, which are measured through optical saturation. It was left a free parameter in order to match the optimal rates measured in Fig. 2 (main text).

The noncollinear hyperfine interaction constant $A_{nc} = A_c B_Q/\omega_n$ and quadrupolar interaction angle θ are determined by fitting the sideband spectrum in Fig. 3d (main text), where we measure the ratio of population $\eta_1 = (\sqrt{3N/4})(A_{nc}/\omega_n)\sin(2\theta)$ on the first sideband ($I_z \rightarrow I_z \pm 1$) and $\eta_2 = (\sqrt{3N/4})(A_{nc}/\omega_n)\cos^2(\theta)/2$ on the second sideband ($I_z \rightarrow I_z \pm 2$) relative to the principal transition. As noted earlier, this is done with the simplification that the ensemble is made up of a single species, *As*, with a Zeeman

energy at 3 T of 21.6 MHz. From this fit we obtain $\eta_1 = 0.10$ and $\eta_2 = 0.14$, or equivalently $B_{\mathrm{Q}} = 1.7$ MHz, and $\theta = 21^\circ$.

We also measure the value $\eta = (\sqrt{3N/4})(A_{\mathrm{nc}}/\omega_{\mathrm{n}})\sin(2\theta)$ directly as determined by measuring the ratio of oscillation frequency of electronic population on the second sideband $I_{\mathrm{z}} \rightarrow I_{\mathrm{z}} + 2$ relative to the frequency on the principal transition Ω_s/Ω (Fig. 4 main text), from which we obtain $\eta = 0.15$.

The discrepency between the sideband-resolved spectra, where $\eta = 0.10 - 0.15$, and the cooling model, where $\eta = 0.06$, may be attributed to deviations from simple spectral broadening of the sidebands in the case of cooling, whenever multiple species with different coupling strength are corralled to participate in the polarization-changing processes, contrary to our simple single-species model.

10.1 Note on electron excited-state population

In Figs. 3 and 4 (main text) we present measurements of the electron excited-state population, which we perform experimentally by measuring the average trion fluorescence following a spin-selective resonant laser pulse. For best agreement with our theoretical analysis in Figs. 3 and 4 (main text), we have found that we needed to leave the conversion factor from readout fluorescence to population as a free parameter. In both figures, this conversion factor is fitted to 60% of the value that would be expected from taking the resonantly driven electron population to be 0.5 at driving times well beyond its coherence time T_2.